JGR Space Physics

RESEARCH ARTICLE
10.1029/2024JA032719

Key Points:

- We investigate cross-field diffusive transport for the mixing of cold low-latitude mantle ions and hot plasma sheet ions observed by MMS
- The waves around the separatrix between the low-latitude mantle and plasma sheet show the characteristics of kinetic Alfvén waves (KAWs)
- Estimated diffusive transport rates through KAWs are sufficiently large to cause the observed ion mixing

Supporting Information:

Supporting Information may be found in the online version of this article.

Correspondence to:

C.-P. Wang,
cat@atmos.ucla.edu

Citation:

Wang, C.-P., Johnson, J. R., Xing, X., Avanov, L. A., Wei, H. Y., & Ahmadi, N. (2024). Ion diffusive transport across the separatrix between the low-latitude mantle and the plasma sheet by kinetic Alfvén waves: MMS observation. *Journal of Geophysical Research: Space Physics*, *129*, e2024JA032719. https://doi.org/10.1029/2024JA032719

Received 3 APR 2024
Accepted 4 OCT 2024

Ion Diffusive Transport Across the Separatrix Between the Low-Latitude Mantle and the Plasma Sheet by Kinetic Alfvén Waves: MMS Observation

Chih-Ping Wang[1], Jay R. Johnson[2], Xiaoyan Xing[3], Levon A. Avanov[4], H. Y. Wei[5], and Narges Ahmadi[6]

[1]Department of Atmospheric and Oceanic Sciences, University of California, Los Angeles, CA, USA, [2]School of Engineering, Andrews University, Berrien Springs, MI, USA, [3]XS Research LLC, Wilmette, IL, USA, [4]Goddard Space Flight Center, NASA, Greenbelt, MD, USA, [5]Department of Earth, Planetary, and Space Physics, University of California, Los Angeles, CA, USA, [6]LASP, University of Colorado Boulder, Boulder, CO, USA

Abstract To understand the entry of the cool low-latitude mantle ions into the tail plasma sheet near the flanks under persistent interplanetary magnetic field B_y, we evaluate the role of the cross-field diffusive transport by kinetic Alfvén waves (KAWs) by investigating two events observed by multiscale (MMS) spacecraft. Around the separatrix between the open and closed field-line regions, a two-component mixing of hot plasma sheet ions of a few keV with cool mantle ions of a few hundred eV was observed, indicating transport across the separatrix. The waves observed between 0.01 and 10 Hz around the separatrix had characteristics consistent with those of KAWs. The consistency allowed us to estimate the wave vectors as a function of frequency by fitting KAW dispersion to the observations. Using the observed wave powers, plasma moments, and the estimated wave vectors, we computed the cross-field diffusion rates associated with KAWs. The diffusion rates were found to be comparable to or larger than the Bohm diffusion rates during the intervals when the two-component mixing was observed, indicating that the KAW diffusive transport can play a role in the entry of low-latitude mantle ions into the plasma sheet.

1. Introduction

Plasma from the solar wind and ionosphere are the two major particle sources for the Earth's magnetosphere. Depending on the interplanetary magnetic field (IMF) orientation (Wing et al., 2014), solar wind particles can enter the magnetosphere via different mechanisms and routes. During southward IMF, the solar wind plasma first enters the high-latitude tail lobes through the cusp and forms high-latitude mantle plasma (e.g., Trainer et al., 2021), then these high-latitude mantle particles $E \times B$ drift toward the current sheet and enter the tail plasma sheet (e.g., Ashour-Abdalla et al., 1993). During northward IMF, plasma can enter into the plasma sheet from the flanks through processes including Kelvin-Helmholtz instability (e.g., Nykyri & Otto, 2001; Otto & Fairfield, 2000) or wave diffusion (e.g., Chaston et al., 2008; Johnson & Cheng, 1997; Johnson & Wing, 2009), or enter through high-latitude double cusp reconnection (e.g., Crooker, 1992; Li et al., 2005, 2009; Raeder et al., 1995). When the IMF B_y component becomes more substantial relative to IMF B_z, the solar wind particles can enter the tail lobe at low latitudes through the open flank magnetopause and form the low-latitude mantle (e.g., Grzedzielski & Macek, 1988; Pilipp & Morfill, 1978; Sibeck & Lin, 2014; Siscoe & Sanchez, 1987). The resulting low-latitude mantle plasma is magnetosheath-like plasma flowing tailward along the open magnetic field lines but with reduced density and tailward speed than the adjacent magnetosheath. The location of low-latitude mantle depends on the direction of IMF B_y. It is formed in the southern (northern) lobe on the dusk-side (dawnside) when IMF B_y is positive and the asymmetry switches to the opposite sense when IMF B_y is negative (e.g., Gosling et al., 1984, 1985; Haerendel & Paschmann, 1975; Hardy et al., 1975, 1976, 1979; Maezawa & Hori, 1998; Siscoe et al., 1994; Taguchi et al., 2001; Wang et al., 2014, 2022; Wang & Xing, 2021). Previous simulation and observation studies have shown that the low-latitude mantle may come into direct contact with the plasma sheet throughout a large portion of the tail from the near-Earth to the mid-tail (Wang & Xing, 2021; Wang et al., 2022). Also, across this interface between the mantle and plasma sheet, the observation studies have shown that a two-component mixture of the cooler and tailward flowing mantle ions and the hotter and isotropic plasma sheet ions can sometimes exist, which is an indication of cross-field transport across the separatrix between the open and closed field-line regions. In addition to tail reconnection, diffusive transport by kinetic Alfvén waves (KAWs) (Johnson & Cheng, 1997) has been suggested as a potential mechanism since intensive electromagnetic ultralow-frequency waves were observed around the separatrix (Wang & Xing, 2021). Therefore, this study is to evaluate such diffusive transport by analyzing the plasma and waves around the separatrix observed by Magnetospheric Multiscale (MMS) spacecraft and estimating the diffusion rates. For the two events presented here, we found that the waves had the characteristics of KAWs and the estimated diffusion rates were sufficiently large to explain the two-component mixing. This paper is organized as follows. In Section 2, we describe the MMS and IMF data. The first event and details of our analysis are presented in Section 3. The analysis results for the sconed event are summarized in Section 4. Summary and discussion are given in Section 5.

2. MMS and IMF Data

MMS is a four-spacecraft constellation (Tooley et al., 2016). The spacecraft is at a low inclination orbit (28.5°) with an apogee of ∼25 R_E and an orbital period of ∼3 days in 2017–2018 (the apogee was later raised to ∼29.3 R_E with an orbital period of 3.5 days). Ions from 10 eV to 30 keV (sample per 4.5 s) are measured by Dual Ion Spectrometers (DIS) of Fast Plasma Investigation (FPI; Pollock et al., 2016). The electric and magnetic fields are measured by FIELDS instrument (Torbert et al., 2016) with the electric fields (32 samples/s) measured by Axial and Spin-plane Double-Probe electric-field sensors (ADP and SDP) and the magnetic fields (16 samples/s) measured by two flux-gate magnetometers (AFG and DFG). These data from the fast survey mode are used. For the IMF conditions, we use the magnetic fields measured by from Acceleration Reconnection Turbulence and Electrodynamics of Moon's Interaction with the Sun (ARTEMIS; Angelopoulos, 2011; Sibeck et al., 2011) when the spacecraft was within the solar wind region. The ARTEMIS magnetic fields (∼4 s resolutions) are measured by the fluxgate magnetometer (FGM) instrument (Auster et al., 2008). The geocentric solar magnetic (GSM) coordinates are used.

We investigate two events when IMF conditions were relatively steady and MMS stayed a considerable amount of time around the separatrix between the low-latitude mantle and the plasma sheet. These conditions allowed for a longer period of steady background magnetic fields for the wave analysis. In both events, the IMF B_y remained positive and MMS spacecraft were below the current sheet near the dusk flank where the low-latitude mantle was expected to appear. The IMF B_z remained negative during the first event while it was positive during the second event.

3. MMS Event 1

We present in this section the analysis of event 1 on 3 October 2021 with detailed descriptions of the methodology used.

3.1. Event 1 Overview

We first present in Figure 1 the overview of event 1 on 3 October 2021 from 04:17 to 04:42 UT. The IMF shown in Figure 1a was measured by ARTEMIS P1 in the upstream solar wind at $X \sim 42$ and $Y \sim 37$ R_E with the yellow-shaded area indicating the interval of event 1. Before the event, the IMF has become relatively steady after ∼03:55 UT. Throughout the event, IMF B_y remained positive at ∼2 nT and IMF B_z remained negative at ~ -3 nT. Figures 1b–1j show fields and plasma observed by MMS-3 near the dusk flank at $X \sim -9$ R_E and $Y \sim 17$ R_E (see the locations at the bottom of Figure 1). MMS was below the current sheet as indicated by the negative B_x (Figure 1b) moving from the lobe/mantle with low ion plasma beta (β_i, Figure 1h) to the plasma sheet with relatively higher $\beta_i > 1$. The intervals of the lobe/mantle and plasma sheet are indicated by the blue and red bars, respectively, on the top of Figure 1b. The region of the plasma sheet in this study is defined by the appearance of isotropic electrons above 1 keV (Figure 1e). This isotropic plasma sheet electrons are shown in detail later in Figure 2f. The first separatrix between the lobe/mantle and the plasma sheet encountered by MMS was at ∼04:26 UT. It can be seen in the ion omnidirectional energy spectrum (Figure 1d), MMS observed cool (a few hundreds of eV) single-component low-latitude mantle ions in the lobe before ∼04:24 UT and hot (a few keV) single-component plasma sheet ions after ∼04:39 UT, and, in between, two-component ions with the mixing of the cool and hot populations. Details of the particle pitch-angle distributions are presented in Section 3.2. The cool low-latitude mantle ion population had density (N_i) of ∼0.2–0.7 cm^{-3} (Figure 1f) and temperature (T_i) of ∼0.1–0.3 keV (Figure 1g), and its bulk flow was tailward with $V_x \sim -50$ to -100 km/s and mainly in the field-aligned direction (Figure 1i). In comparison, the hot plasma sheet ion population had N_i of ∼0.2 cm^{-3}, T_i of ∼2 keV, and

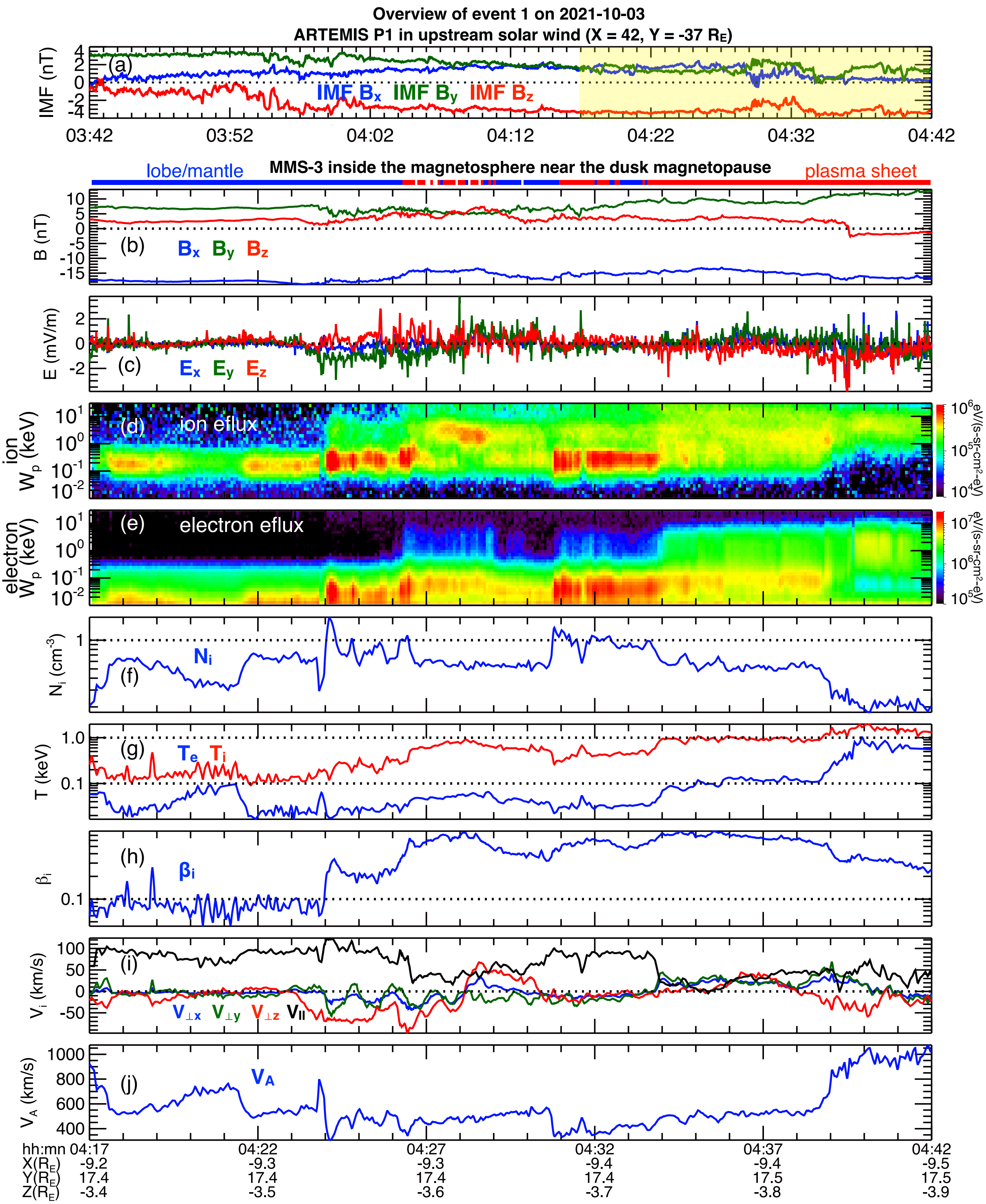

Figure 1. Overview of event 1 on 3 October 2021. (a) Interplanetary magnetic field observed by ARTEMIS P1. The yellow-shaded duration indicates the interval of event 1. (b–j) MMS-3 observations of panel (b) magnetic fields, (c) electric fields, energy spectrum of panel (d) ion and (e) electron omnidirectional energy fluxes, (f) ion density, (g) ion and electron temperatures, (h) ion plasma beta, (i) ion bulk perpendicular and parallel velocities, and (j) Alfvén speed. The regions encountered by MMS are indicated on the top by the blue (red) bars for lobe/mantle (plasma sheet).

10.1029/2024JA032719

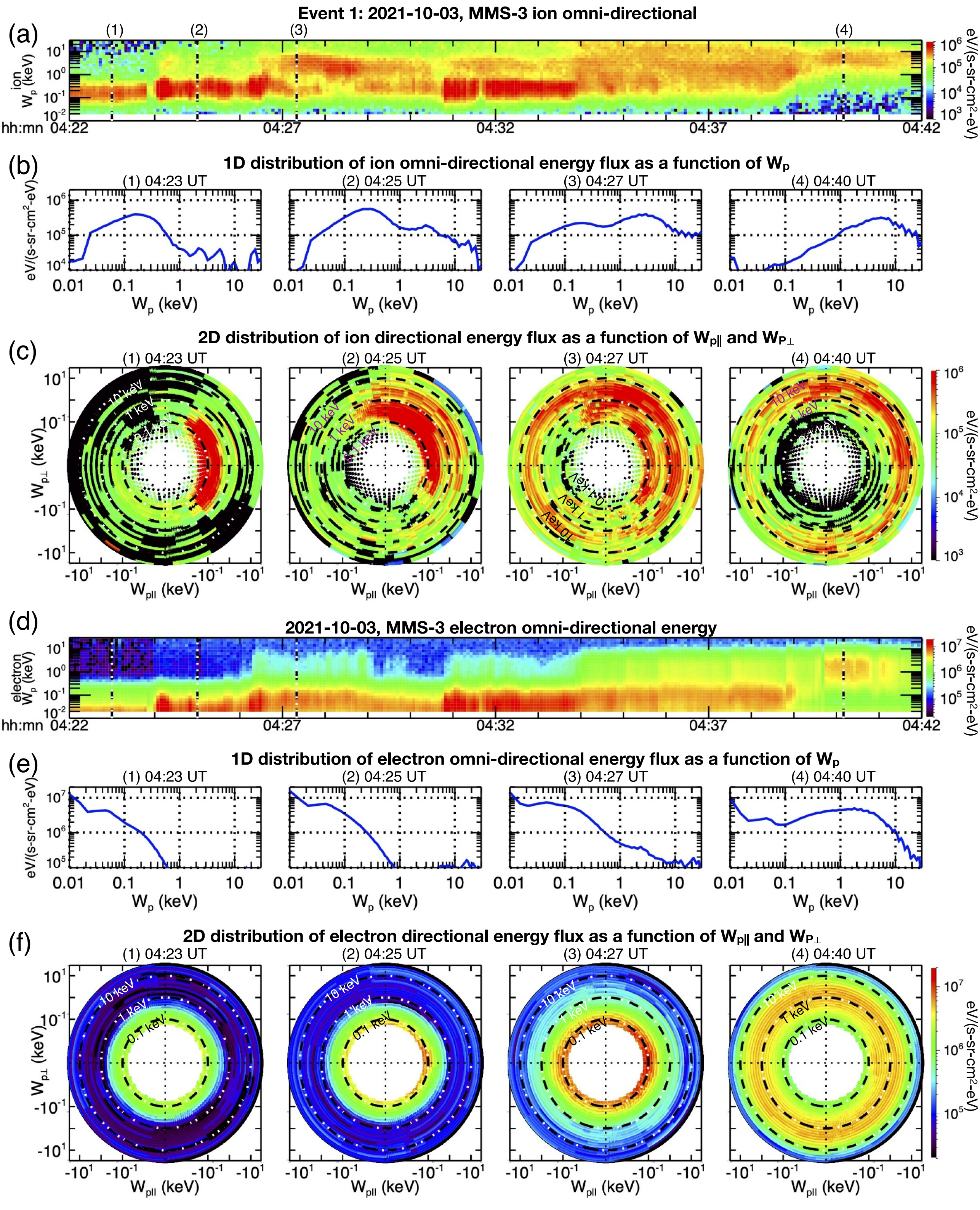

Figure 2. Particle distributions for event 1 on 3 October 2021. Energy spectrum of panels (a) ion and (d) electron omnidirectional energy fluxes. 1D omnidirectional energy fluxes for panels (b) ions and (e) electrons, and 2D distributions of directional energy fluxes for panels (c) ions and (f) electrons at four different times ((1) 04:23, (2) 04:25, (3) 04:27, and (4) 04:40 UT) indicated on the top of panel (a) and by the vertical dotted lines.

slow bulk flow speed of <50 km/s. The electron temperature (T_e, Figure 1g) was about a factor of ∼10 lower than T_i during the intervals of the lobe/mantle and the mixing and a factor of ∼3 lower than T_i when there was only the presence of the single-component hot plasma sheet ions. Note that both the ions and electrons immediately on the plasma sheet side of the separatrix (the plasma sheet boundary layer) did not show any signatures, such as energy dispersion and high-speed ion flows, indicating the magnetic field lines around the separatrix were connected to a tail reconnection region as reported in other studies (e.g., Sergeev et al., 2021; Wellenzohn et al., 2021). The Alfvén speed was several hundreds of km/s and was lower in the presence of the cool ions (Figure 1j). Substantial fluctuations were observed in both the magnetic and electric fields around the mantle/plasma sheet interface from ∼04:24 to 04:34 UT (Figures 1b and 1c). Wave analysis of these fluctuations presented in Section 3.3 shows that KAW was the dominant wave mode. The wave vectors estimated using the four MMS spacecraft are shown in Section 3.4 and the cross-field diffusion rates associated with KAWs are presented in Section 3.5.

3.2. Ion and Electron Particle Distributions

We compare in Figure 2 the particle distributions in different regions (the lobe, the region of ion mixing, and the plasma sheet). The time series of energy spectrum of omnidirectional energy fluxes are shown in Figures 2a and 2d for ion and electron, respectively. The 1D distributions of omnidirectional ion energy fluxes and the 2D distributions of directional ion energy fluxes are shown in Figures 2b and 2c, respectively, at four different times/regions (indicated by the numbers on the top of Figure 2a): (1) the single-component ions within the lobe/mantle at 04:23 UT, (2) the two-component ions in the mixing region on the lobe side at 04:25 UT, (3) the two-component ions in the mixing region on the plasma sheet side at 04:27 UT, and (4) the single-component ions within the plasma sheet at 04:40 UT. The particle's kinetic energy is $W_p = 1/2mV_p^2$, where m is the particle mass and V_p is the particle's velocity. Note that the 2D distributions are shown in $W_{p,\parallel}$–$W_{p,\perp}$ and we assign positive (negative) values to $W_{p,\parallel}$ to indicate the corresponding positive (negative) direction of $V_{p,\parallel}$ (the same direction notation for $W_{p,\perp}$). The 1D and 2D distributions of electron energy fluxes for these times are shown in Figures 2e and 2f, respectively. In the 04:23 UT plots, the cool field-aligned tailward flowing mantle ions are indicated by the single-component ion fluxes peaking at ∼0.2 keV and around the $+V_{p,\parallel}$ direction (note that the parallel direction was tailward because MMS was in the southern lobe at the time). In comparison, in the 04:40 UT plots, the hot isotropic plasma sheet ions are indicated by the single-component ions peaking at ∼7 keV at all pitch angles. Similarly, Figure 2f shows that isotropic electrons of ∼2 keV were seen in the plasma sheet but not in the lobe. For the two-component ions in the 04:25 and 04:27 UT plots, the cool component at ∼0.2 keV in the $+V_{p,\parallel}$ direction was similar to the single-component low-latitude mantle ions seen in the 04:23 UT plot, while the hot component ions peaking at a few keV was similar to the single-component plasma sheet ions seen in the 04:40 UT plot. However, the hot component ions were highly isotropic in the 04:27 UT plot but highly anisotropic in the 04:25 UT plot. Isotropic keV electrons were only seen in the 04:27 UT plot but not in the 04:25 plot. These indicate that the ion two-component mixing shown in Figure 2a occurred across the separatrix from the lobe/mantle side (open field-line region) to the plasma sheet side (closed field-line region).

3.3. Kinetic Alfvén Waves and Wave Vector Estimation

We show in Figure 3 that the electric and magnetic fluctuations around the separatrix observed by MMS 3 had the characteristics of KAWs and we estimate the wave vectors by fitting KAWs to the observed waves in Figure 4. The ion omnidirectional energy spectrum across the separatrix is shown in Figure 4a (note that the separatrix was at ∼04:26 UT). The magnetic and electric field components in the mean field-aligned (MFA) coordinates are shown in Figure 3 for $B_\parallel$ in the mean-field direction, and Figures 3d and 3f for $B_\perp$ and $E_\perp$ in the perpendicular direction, respectively. The mean magnetic field $\mathbf{B}_0$ is defined in this study as the 2-min running averages of the magnetic fields. The first perpendicular direction (⊥1) is defined as the cross product of the parallel direction and the azimuthal direction ($\mathbf{A} \equiv (Y_{sc}, -X_{sc}, 0)/r_{xy}$, where X_{sc} and Y_{sc} are the spacecraft's location and $r_{xy}{}^2 = X_{sc}{}^2 + Y_{sc}{}^2$), and the second perpendicular direction (⊥2) completes the orthogonal right-hand system. The power spectrum densities (PSDs) of $B_\parallel$, $B_\perp$, and $E_\perp$ within the spacecraft frequency (f_{sc}) range of 0.01–8 Hz are shown in Figures 3c, 3e, and 3g, respectively, with proton cyclotron frequency (f_{cp}) indicated by the black curve. We show in Figures 3i–3o the comparisons between the PSDs of $B_\parallel$, $B_\perp$, and $E_\perp$ for three selected 10-s intervals, as indicated on the top of Figure 3a: (1) 04:25:05–04:25:15 UT on the lobe/mantle side, (2) 04:25:55–04:26:05 UT at the separatrix, and (3) 04:27:05–04:27:15 UT on the plasma sheet side. As shown in Figures 3i, 3k, and 3n, for all three intervals, the PSDs of $B_\perp$ (blue) were relatively larger than that of $B_\parallel$ (green). There appeared to be

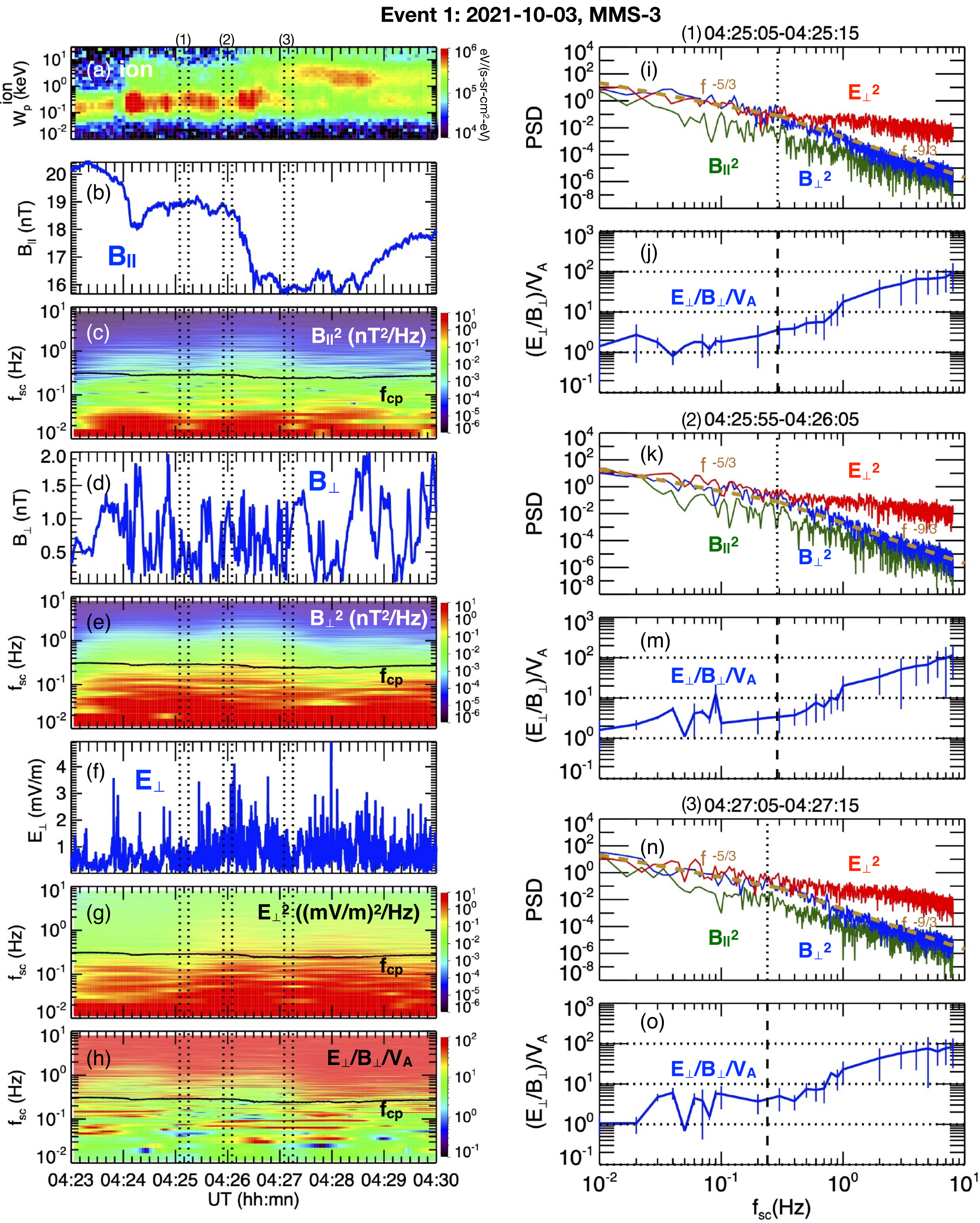
Event 1: 2021-10-03, MMS-3
(1) 04:25:05-04:25:15
(2) 04:25:55-04:26:05
(3) 04:27:05-04:27:15
(a) ion
(b) B∥
(c) B∥² (nT²/Hz)
(d) B⊥
(e) B⊥² (nT²/Hz)
(f) E⊥
(g) E⊥² ((mV/m)²/Hz)
(h) E⊥/B⊥/VA
fcp
UT (hh:mn)
PSD
(E⊥/B⊥)/VA
fsc(Hz)
f -5/3
f -9/3
E⊥²
B∥²
B⊥²
E⊥/B⊥/VA

Figure 3.

a change in the frequency spectrum of the PSD of $B_\perp$ with the spectrum approximately following the power law of $f^{-5/3}$ ($f^{-9/3}$) (indicated by the brown dashed line) at frequencies lower (higher) than f_{cp} (indicated by the vertical dotted line). The changes in the power law index value indicated the magnetic turbulence cascade from the magnetohydrodynamic scale to the sub-ion scale. The PSDs of $E_\perp$ (red) were comparable to that of $B_\perp$ (blue) at frequencies lower than f_{cp}. But at frequencies higher than f_{cp}, $E_\perp$ became increasingly larger than $B_\perp$ with increasing frequency. As a result, as can be seen in Figures 3j, 3m, and 3o, the ratio of $E_\perp/B_\perp/V_A$ was closer to 1 at smaller f_{sc} near 0.01 Hz and the ratio increased with increasing f_{sc} to ∼100 at 8 Hz. This dispersion feature indicated that the waves were dominantly KAWs.

We can estimate the wave vectors by fitting the KAW dispersion to the observed $E_\perp/B_\perp/V_A$ ratio. For KAWs with wave vector k and wave normal angle θ_W, the dispersion is given by the solution of,

$$k_\parallel^2 V_A^2 k_\perp^2 \rho_s^2 = \left(\omega^2 - \frac{k_\parallel^2 V_A^2}{\chi_i}\right) \cdot \left[1 - \frac{k_\parallel^2 V_s^2}{\omega^2} I_0(\alpha_i)\, e^{-\alpha_i}\right]$$

where $k_\perp = \sin(\theta_W)$, $k_\parallel = cos(\theta_W)$, V_A is the Alfvén speed, ρ_s is the ion acoustic gyro-radius, V_s is the acoustic speed, $\chi_i = [1 - I_0(\alpha_i)\, e^{-\alpha_i}]/\alpha_i$, $\alpha_i = {k_\perp}^2{\rho_i}^2$, and I_0 is the zero-order modified Bessel function and ρ_i is the ion gyro-radius (Chaston et al., 2005, 2008). The ratio of $E_\perp/B_\perp$ from KAW is

$$\frac{E_\perp}{B_\perp} = -\frac{\omega}{k_\parallel}\left[1 + \frac{k_\perp^2 \rho_s^2 \chi_i}{1 - I_o(\alpha_i) e^{-\alpha_i \frac{k_\parallel^2 V_s^2}{\omega^2}}}\right]^{-1}$$

Note that, different from the classical KAW dispersion, the above KAW dispersion includes ion motion along the magnetic field, thus, the ion parallel current for finite plasma beta introduces the dependency of the $E_\perp/B_\perp$ ratio on $k_\parallel$ and ω. We show in Figure 4 how we conduct a grid search in the [$k_\parallel$, $k_\perp$] space to find the optimal ($k_\parallel$, $k_\perp$) combinations that give a reasonably good fit of the KAW dispersion to the observations. This technique has been used in Chaston et al. (2014). We assume that $k_\parallel$ is independent of f_{sc} and search the $k_\parallel$ range from 5×10^{-6} to 5×10^{-4} km^{-1}, as shown in Figure 4a. On the other hand, we assume that $k_\perp$ increases with increasing f_{sc} by utilizing the Taylor hypothesis, $k_T = 2\pi f_{sc}/V_{i\perp}$, where $V_{i\perp}$ is the perpendicular ion bulk flow speed. We use the observed $V_{i\perp}$ speeds. Thus, we assume $k_\perp = R_k\, k_T$, where R_k is a constant. As shown in Figure 4g, we search the $k_\perp$ range from $R_k = 1$ to 10. To provide a better picture of how the KAW wave parameters depend on $k_\parallel$ and $k_\perp$, we show the grid search results in two groups: Figures 4a–4e show how the wave parameters vary with different $k_\parallel$ values at fixed $k_\perp = k_T$, and Figures 4f–4j show the variations with different $k_\perp$ values at fixed $k_\parallel = 5 \times 10^{-5}$ km^{-1}. Each light blue curve corresponds to a ($k_\parallel$, $k_\perp$) combination. We also plot two curves in green and magenta to indicate those with the lowest and highest k values (the values are indicated on the plots), respectively, and a red curve to indicate that with the median k values ($k_\parallel = 5 \times 10^{-5}$ and $R_k = 1$). Note that for V_A, V_s, ρ_i, and ρ_s, we compute them using the observed values averaged within a 10-s window (e.g., 04:25:05–04:25:15 UT in Figures 4a–4o). Figures 4c and 4h show that θ_W increases with increasing f_{sc} and approaches 90°, and larger $k_\parallel$ or smaller R_k corresponds to lower θ_W. Figures 4d and 4i show that ω increases with increasing f_{sc} and approaches $\omega_{cp} = 2\pi f_{cp}$ (the horizontal dashed line), and larger $k_\parallel$ or larger R_k corresponds to larger ω. Figure 4e shows that the $k_\parallel$ value only affects the $E_\perp/B_\perp/V_A$ ratio at $f_{sc} > f_{cp}$ (the vertical dashed line) while Figure 4j shows that the $k_\perp$ value affects the ratio at all f_{sc} with the largest effect around f_{cp}. To determine which ($k_\parallel$, $k_\perp$) combinations give an optimal fit to the observation, we evaluate the difference between the observed $E_\perp/B_\perp/V_A$ ratio, R_{obs}, and the KAW ratio, R_{KAW}, using NRMSE (normalized root-mean-square error) defined as $\sum(R_{obs} - R_{KAW})^2/\langle R_{obs}\rangle$, where $\langle R_{obs}\rangle$ is the average of R_{obs}. The blue curve in Figures 4e and 4j shows R_{obs} for 04:25:10 UT (the same as that shown in Figure 3j) and the green, red, and magenta curves show the R_{KAW} corresponding to the three

Figure 3. Wave analysis for MMS3 field fluctuation for event 1 on 3 October 2021. (a) Energy spectrum of ion omnidirectional energy fluxes. (b) $B_\parallel$, (d) $B_\perp$, and (f) $E_\perp$ in the mean field-aligned coordinates. Power spectrum density (PSD) of (c) ${B_\parallel}^2$, (e) ${B_\perp}^2$, (g) ${E_\perp}^2$, and (h) the $E_\perp/B_\perp/V_A$ ratio as a function of f_{sc}. The black curves in (c, e, g, h) indicate the proton cyclotron frequency (f_{cp}). The three 10-s intervals (1)–(3) are indicated in the top of (a) and the wave spectrum are shown in panels (i–j) for interval (1), in panels (k–m) for interval (2), and in (n–o) for interval (3). (i, k, and n) The PSD of ${B_\perp}^2$ (blue), ${B_\parallel}^2$ (green) and ${E_\perp}^2$ (red). The brown dashed line below (above) f_{cp} (indicated by vertical dashed line) indicates $f^{-5/3}$ ($f^{-9/3}$). (j, m, and o) The ratio of $E_\perp/B_\perp/V_A$.

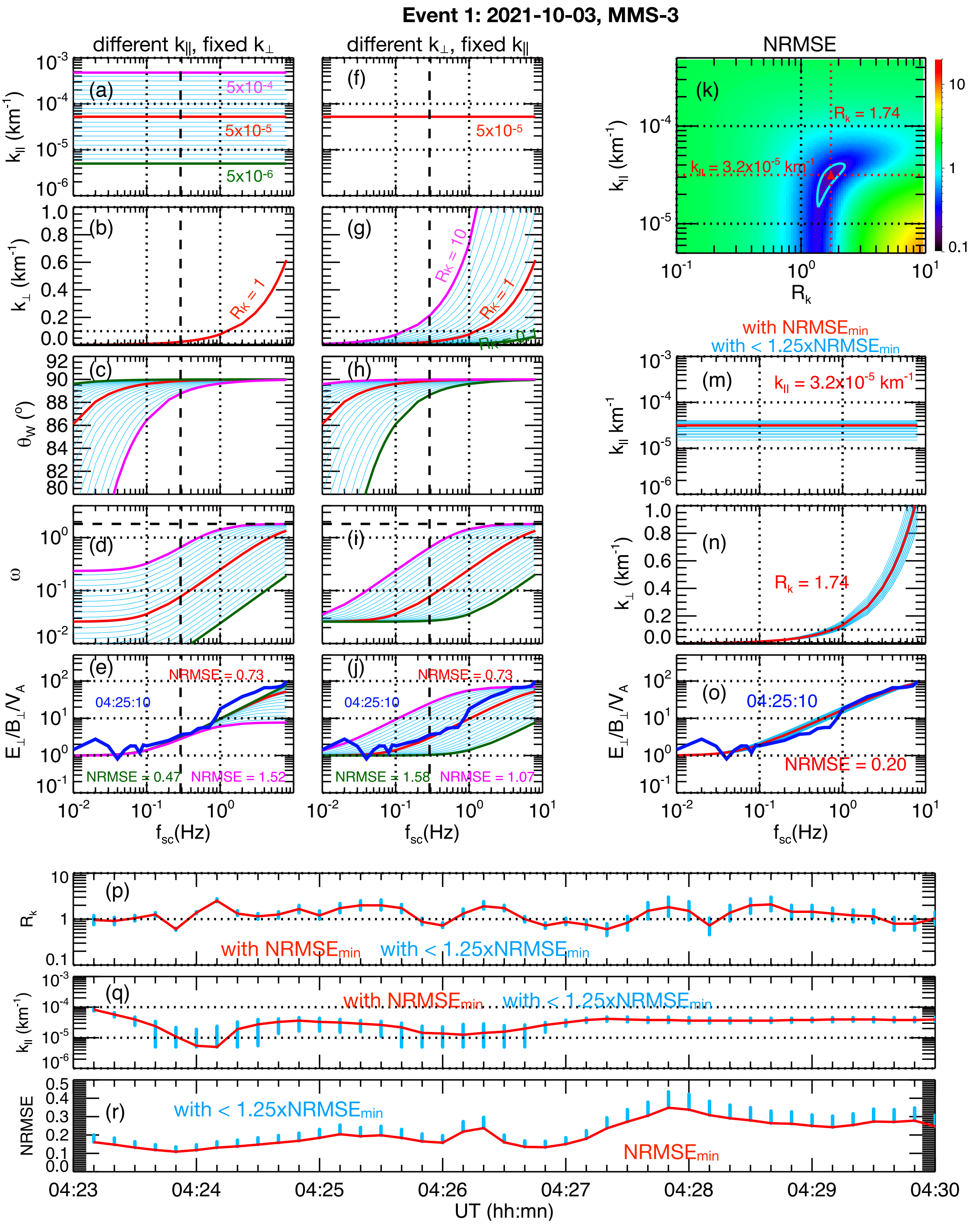

Event 1: 2021-10-03, MMS-3
different k||, fixed k⊥
different k⊥, fixed k||
NRMSE
(a)
(b)
(c)
(d)
(e)
(f)
(g)
(h)
(i)
(j)
(k)
(m)
(n)
(o)
(p)
(q)
(r)
5x10-4
5x10-5
5x10-6
Rk = 1
Rk = 10
Rk = 0.1
Rk = 1.74
k|| = 3.2x10-5 km-1
NRMSE = 0.73
NRMSE = 0.47
NRMSE = 1.52
NRMSE = 1.58
NRMSE = 1.07
NRMSE = 0.20
04:25:10
with NRMSEmin
with < 1.25xNRMSEmin
NRMSEmin
k|| (km-1)
k⊥ (km-1)
θW (°)
ω
E⊥/B⊥/VA
fsc(Hz)
Rk
NRMSE
UT (hh:mn)
04:23
04:24
04:25
04:26
04:27
04:28
04:29
04:30

Figure 4.

selected ($k_{\parallel}$, $k_{\perp}$) combinations with their NRMSE values indicated. Visual inspection of these curves shows that the combination with lower NRMSE has a better fit to the observation. Figure 4k shows the NRMSE values in comparison with the R_{obs} at 04:25:10 UT for all ($R_{\text{T,}}$ $k_{\parallel}$) combinations with the red triangle indicating the minimum of NRMSE ($\text{NRMSE}_{\text{min}}$), the red horizontal (vertical) dotted line indicating the corresponding R_{k} and $k_{\parallel}$, respectively, and the light blue contour indicating $1.25 \times \text{NRMSE}_{\text{min}}$. Figures 4m–4o show the $k_{\parallel}$, $k_{\perp}$, and R_{KAW}, respectively, for the combination with $\text{NRMSE}_{\text{min}}$ (the red curve) and the combinations with $\text{NRMSE} \leq 1.25 \times \text{NRMSE}_{\text{min}}$ (the light blue curves). As shown in Figure 4o, these ($k_{\parallel}$, $k_{\perp}$) combinations give fits reasonably close to the R_{obs} values (blue). Hence, we use the ($k_{\parallel}$, $k_{\perp}$) combination corresponding to $\text{NRMSE}_{\text{min}}$ as the estimated optimal wave vectors for KAWs and choose the ($k_{\parallel}$, $k_{\perp}$) values with NRMSE within $\leq 1.25 \times \text{NRMSE}_{\text{min}}$ to indicate the uncertainty of the estimation. We conduct the grid search to find the optical wave vectors for all other intervals around the separatrix from 04:23 to 04:30 UT (see Figure S1 in Supporting Information S1 for the comparison between R_{obs} and R_{KAW} for other intervals) and the estimated R_{k}, $k_{\parallel}$, and their NRMSE are shown in Figure 4p–4r, respectively. The estimated $k_{\perp}$ values were found to be in the vicinity of k_{T}, indicating that the Taylor hypothesis was a good approximation. The majority of the estimated $k_{\parallel}$ values were within $1 \sim 5 \times 10^{-5}$ km^{-1}. This $k_{\parallel}$ range corresponds to the parallel wave lengths of ∼3–15 R_{E}, which is comparable to the spatial scale of the separatrix in the X direction. These estimated wave vectors are used in computing the diffusion coefficients in Section 3.5.

3.4. Evaluation of the Taylor Hypothesis Using Four Spacecraft

In this section, we show that the Taylor Hypothesis was a good approximation by evaluating it with wave vectors estimated using the multi-spacecraft timing method (Russell et al., 1983; Schwartz, 1998; Zhang et al., 2022). For a propagating wave with a single-frequency (f) observed by the four spacecraft at different locations ($\mathbf{r}$) and times, its average phase velocity over time taken during the time delay and the space between the spacecraft, $\mathbf{v_w}(f, t)$, can be estimated with

$$\begin{pmatrix} \Delta\mathbf{r}_{12} \\ \Delta\mathbf{r}_{13} \\ \Delta\mathbf{r}_{14} \end{pmatrix} \cdot \frac{1}{|v_{\text{w}}(\text{f, t})|} \begin{pmatrix} n_{\text{x}} \\ n_{\text{y}} \\ n_{\text{z}} \end{pmatrix} = \begin{pmatrix} \Delta t_{12} \\ \Delta t_{13} \\ \Delta t_{14} \end{pmatrix}$$

where $(n_{\text{x}}, n_{\text{y}}, n_{\text{z}}) = \mathbf{n}$ is the wave propagation direction and $\Delta\mathbf{r}_{12}$, $\Delta\mathbf{r}_{13}$, $\Delta\mathbf{r}_{14}$, Δt_{12}, Δt_{13}, and Δt_{14} are the separations in space and time between a spacecraft pair with the subscript 1, 2, 3, and 4 indicating MMS-1, 2, 3, and 4, respectively. We can solve this for $(1/\text{v}_{\text{w}})\mathbf{n}$.

$$\left(\frac{1}{v_w}\right)\mathbf{n} = \begin{pmatrix} \Delta\mathbf{r}_{12} \\ \Delta\mathbf{r}_{13} \\ \Delta\mathbf{r}_{14} \end{pmatrix}^{-1} \begin{pmatrix} \Delta t_{12} \\ \Delta t_{13} \\ \Delta t_{14} \end{pmatrix}$$

The wave vector can then be obtained from $\mathbf{k}(f, t) \cdot \mathbf{v_w}(f, t) = 2\pi f$.

Figure 5 shows how we obtain $\mathbf{k}(f, t)$ for f from 0.2 to 2 Hz and t = 04:27:09 UT. The formation of the four MMS spacecraft at 04:27:09 UT is shown in Figure 5a. The formation quality factor (Fuselier et al., 2016) was 0.76–0.83 during this event, indicating a good tetrahedron configuration. Figures 5b and 5c show (ΔX, ΔY) and (ΔX, ΔZ), respectively, of $\Delta\mathbf{r}_{12}$, $\Delta\mathbf{r}_{13}$, $\Delta\mathbf{r}_{14}$, the separations were ∼10–60 km. Figure 5d shows unfiltered profiles of one of the perpendicular component, $\text{B}_{\perp 1}$, observed by the four spacecraft and it is clear that they observed the

Figure 4. Wave vector estimation for kinetic Alfvén waves (KAWs) observed by MMS3 for event 1. Wave parameters for panels (a–e) different $\text{k}_{\parallel}$ and fixed $\text{k}_{\perp}$ and (f–j) different $\text{k}_{\perp}$ and fixed $\text{k}_{\parallel}$, (a and f) $\text{k}_{\parallel}$, (b and g) $\text{k}_{\perp}$ (c and h) θ_{w}, (d and i) ω, and (e and j) $E_{\perp}/B_{\perp}/V_{\text{A}}$ ratio as a function of f_{sc}. Each light blue curve in panels (a–j) corresponds to a ($\text{k}_{\parallel}$, $\text{k}_{\perp}$) combination, and the green, red, and magenta curves correspond to the lowest, median, and highest k values. The blue curve in (e, j, and o) is the ratio observed at 04:25:10 UT. The vertical dashed line indicates f_{cp}. (k) NRMSE contours as a function of R_{k} and $\text{k}_{\parallel}$. The red triangle indicates $\text{NRMSE}_{\text{min}}$ and the red vertical (horizontal) dotted line indicates the corresponding R_{k} and $\text{k}_{\parallel}$, respectively. The light blue contour indicates $1.25 \times \text{NRMSE}_{\text{min}}$. (m) $\text{k}_{\parallel}$, (n) $\text{k}_{\perp}$, and (o) $E_{\perp}/B_{\perp}/V_{\text{A}}$ ratio as a function of f_{sc} for KAWs with $\text{NRMSE}_{\text{min}}$ (red) and $<1.25 \times \text{NRMSE}_{\text{min}}$ (light blue). Temporal variation of the estimated (p) R_{K} and (q) $\text{k}_{\parallel}$, and (r) their NRMSE for KAWs with $\text{NRMSE}_{\text{min}}$ (red) and $<1.25 \times \text{NRMSE}_{\text{min}}$ (light blue).

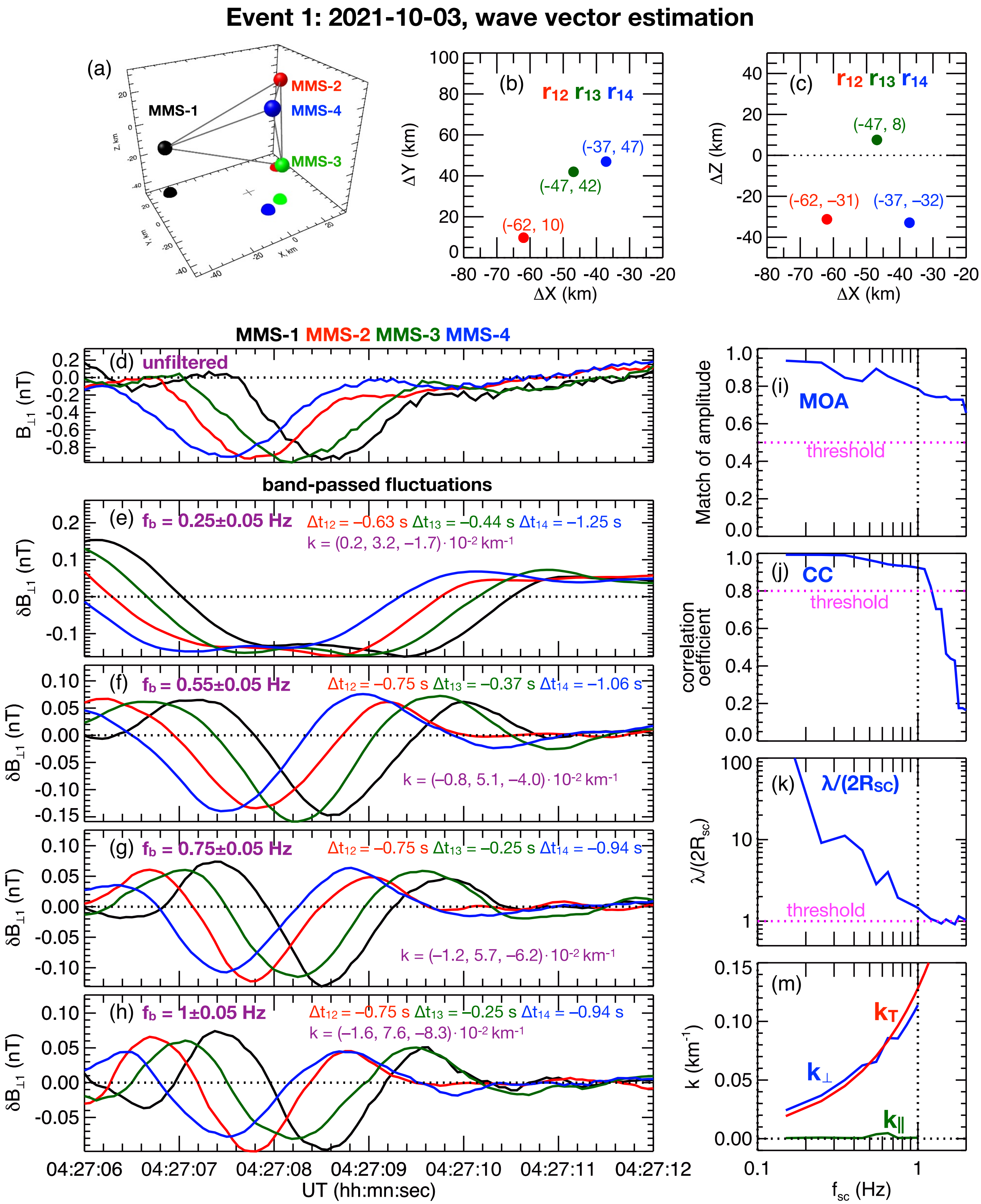
Event 1: 2021-10-03, wave vector estimation
(a)
MMS-1
MMS-2
MMS-4
MMS-3
(b)
r_{12} r_{13} r_{14}
(-37, 47)
(-47, 42)
(-62, 10)
ΔY (km)
ΔX (km)
(c)
r_{12} r_{13} r_{14}
(-47, 8)
(-62, −31)
(-37, −32)
ΔZ (km)
ΔX (km)
MMS-1 MMS-2 MMS-3 MMS-4
(d) unfiltered
$B_{\perp 1}$ (nT)
band-passed fluctuations
(e) f_b = 0.25±0.05 Hz
Δt_{12} = −0.63 s Δt_{13} = −0.44 s Δt_{14} = −1.25 s
k = (0.2, 3.2, −1.7)·10^{-2} km^{-1}
(f) f_b = 0.55±0.05 Hz
Δt_{12} = −0.75 s Δt_{13} = −0.37 s Δt_{14} = −1.06 s
k = (−0.8, 5.1, −4.0)·10^{-2} km^{-1}
(g) f_b = 0.75±0.05 Hz
Δt_{12} = −0.75 s Δt_{13} = −0.25 s Δt_{14} = −0.94 s
k = (−1.2, 5.7, −6.2)·10^{-2} km^{-1}
(h) f_b = 1±0.05 Hz
Δt_{12} = −0.75 s Δt_{13} = −0.25 s Δt_{14} = −0.94 s
k = (−1.6, 7.6, −8.3)·10^{-2} km^{-1}
$\delta B_{\perp 1}$ (nT)
04:27:06 04:27:07 04:27:08 04:27:09 04:27:10 04:27:11 04:27:12
UT (hh:mn:sec)
(i) MOA
threshold
Match of amplitude
(j) CC
threshold
correlation oefficient
(k) $\lambda/(2R_{SC})$
threshold
$\lambda/(2R_{sc})$
(m)
k_T
$k_\perp$
$k_\parallel$
k (km^{-1})
f_{sc} (Hz)

Figure 5.

same wave structure with slight time differences. We use a band-pass filter to obtain the time series of waves at different frequency bands using a bandwidth of 0.1 Hz. Figures 4h–5e show band-passed profiles of $B_{\perp 1}$ for four selected frequency bands. For each frequency, we choose the band-passed data within a 6 s window centered at 04:27:09 UT and examine the cross-correlations of the data with different time shifts between two spacecraft to estimate Δt_{12}, Δt_{13}, and Δt_{14} and the corresponding (k_x, k_y, k_z) (with the values indicated on the plots).

To evaluate the quality of the wave vector estimation shown in Figures 5e–5h, we adapt the three measure parameters and their thresholds used in Zhang et al. (2022): (a) Match of amplitude (MOA) is the ratio of the smallest spectral wave amplitude to the largest spectral wave amplitude among the four spacecraft. This is a measure for all four spacecraft detecting the same wave. (b) The correlation coefficient (CC) is the minimum value of the "Pearson" cross-correlation coefficients after the time shifts. This is used to eliminate the phase difference during the time-shifting processes. (c) Parameter $\lambda/(2R_{SC})$, where $\lambda/2$ is the half-wavelength and R_{SC} is the average separation among the four spacecraft. This is used to ensure that the "time delay" is obtained by monitoring the same wavefront and that there is no uncertainty of several wave periods during the time-shift process. The thresholds for good quality are MOA > 0.5, CC > 0.8, and $\lambda/(2R_{SC}) > 1$. As shown in Figures 5i–5k for MOA, CC, and $\lambda/(2R_{SC})$, respectively, as a function of f_{sc}, the thresholds (indicated by the magenta horizontal dotted lines) were satisfied at < ∼1 Hz. As shown in Figure 5m for the estimated $k_\parallel$ (green), $k_\perp$ (blue curve), and k_T (red curve) as a function of f_{sc}, $k_\perp$ was >> $k_\parallel$, and $k_\parallel$ did not change substantially with f_{sc} while $k_\perp$ increased with increasing f_{sc}. The k_T profile was close to that of $k_\perp$, indicating that the Taylor hypothesis was a good approximation at least for the ∼0.1–1 Hz range.

As shown in Figure 5, the wave vectors we can estimate using the multi-spacecraft method for this event were within a rather limited frequency range, which is not sufficient for evaluating diffusion rates by the waves over the observed frequency range. Thus, for the diffusion rates presented in the next section, we use the wave vectors estimated by the fitting method shown in Figure 4.

3.5. Evaluating Cross-Field Diffusion Rates

In this section, we show that the cross-field diffusion rates associated with the observed KAWs are sufficiently large across the separatrix. We use the wave vectors estimated by fitting KAW dispersion to the observations presented in Section 3.3. From the gyrokinetic equations, the density evolution due to diffusion along the cross-field direction, $x_\perp$, is approximately $\frac{\partial N}{\partial t} = \frac{\partial}{\partial x_\perp} D_W \frac{\partial N}{\partial x_\perp}$, where N is density and D_W is the drift-kinetic diffusion coefficient (e.g., Hasegawa & Mima, 1978; Johnson & Cheng, 1997). Using a quasilinear treatment of the gyrokinetic equation (Chaston et al., 2009; Johnson & Cheng, 1997), the diffusion coefficient for KAWs including magnetic drift effects and full Larmor radius effects assuming a Maxwellian distribution is

$$D_W \approx \sum_{j=1}^{6} \sum_k D_{W,j}(k) = \sum_{j=1}^{6} \sum_k \left(\frac{\pi}{8}\right)^{\frac{1}{2}} \frac{1}{|k_\parallel| V_i} \left(\frac{|E_\perp(k)|}{B_0}\right)^2 d_j = \sum_{j=1}^{6} \sum_k D_0(k)\, d_j$$

where B_0 is the background magnetic field strength and V_i is the ion thermal speed. Here $d_1 = \eta^2 R_{00}{}^0$, $d_2 = \alpha^2(1 + \eta)^2 R_{00}{}^4$, $d_3 = 2(\sigma^2\eta^2)/(k_\perp{}^2\rho_i{}^2) R_{11}{}^2$, $d_4 = -2\alpha\eta(1 + \eta) R_{00}{}^2$, $d_5 = 2^{3/2}(\sigma\eta^2)/(k_\perp\rho_i) R_{10}{}^1$, and $d_6 = -2^{3/2}\sigma\alpha\eta(1 + \eta)/(k_\perp\rho_i) R_{10}{}^3$, where $\alpha = \omega_d/\omega$, $\omega_d = \mathbf{k} V_i \cdot [B/|B| \times \rho_i \nabla \mathbf{B}/B]$ is the magnetic drift frequency, $\eta = -k_\perp E_\parallel / k_\parallel E_\perp$, $\sigma = E_{\parallel TD}/E_\parallel$, where $E_{\parallel TD} \approx -i[m_i V_i{}^2/(2B_0)] k_\parallel B_\parallel(k)/q_i$ is the effective $E_\parallel$ due to the wave ion mirror force ("TD" stands for transient time damping), where m_i is the ion mass and q_i is the ion charge. The ratio of $E_\parallel$ to $E_\perp$ is

$$\frac{E_\parallel}{E_\perp} = -\frac{k_\parallel k_\perp \rho_s^2 \chi_i}{1 - I_o(\alpha_i)\, e^{-\alpha_i \frac{k_\parallel^2 V_s^2}{\omega^2}}}$$

Figure 5. Examine the Taylor hypothesis using four MMS spacecraft for event 1 on 3 October 2021. (a) 3D plot of the MMS formation and the projections of spacecraft in the X-Y plane at 04:50 UT. The space separations between two MMS spacecraft (r_{12}, r_{13}, r_{14}) in the (b) X and Y and (c) X and Z directions. (d) Time series of unfiltered $B_{\perp 1}$ component observed by the four MMS spacecraft. (e–h) Time series of band-passed fluctuations of the $B_{\perp 1}$ component for four selected frequency bands observed by the four MMS. For each band, the values of the frequency band (f_b), the time separation Δt between each MMS pair (t_{12}, t_{13}, t_{14}), and the estimated wave vector, k, are indicated on each plot. (i) Match of amplitude, (j) correlation coefficient (CC), (k) λ/(2Rsc), and (e) the $k_\parallel$, $k_\perp$ and k_T as a function of f_{sc}.

Also

$$R_{nm}^{l} = 2\int_0^\infty dx x^{l+1} J_n(bx) J_m(bx) \exp\left[-x^2 - \left(\zeta - \zeta_d x^2\right)^2\right]$$

where $b = \sqrt{2}k_\perp\rho_i$, $\zeta = \omega/\left(\sqrt{2}\,k_\parallel V_i\right)$, $\zeta_d = \omega_d/\left(\sqrt{2}\,k_\parallel V_i\right)$, and J_n are Bessel functions of order n. The term $D_{W,1}$ is due to Landau damping (LD), $D_{W,2}$ is due to magnetic field gradient drift (GD), $D_{W,3}$ is due to TD, $D_{W,4}$ is due to coupling between GD and LD, $D_{W,5}$ is due to coupling between TD and LD, and $D_{W,6}$ is due to coupling between GD and TD. Note that the $D_{W,2}$, $D_{W,4}$ and $D_{W,6}$ associated with the magnetic drift includes only the effect of the GD, not the curvature drift. As discussed in Section 5, including the curvature drift might potentially weaken the effect of the GD. Considering this uncertainty in the contribution by the magnetic drift, we also compute the total diffusion rate without the effect of magnetic drift, that is, the rate due to LD and TD, $D_{W(LD+TD)} = D_{W,1} + D_{W,3} + D_{W,5}$.

Figure 6a shows the PSD of observed $B_\perp$, $B_\parallel$, and $E_\perp$, as well as computed $E_\parallel$ and $E_{\parallel TD}$, as a function of k from MMS3 for the interval of 04:27:05-04:27-15 UT (the same as interval (3) shown in Figure 3n) and Figure 6b shows the corresponding $|D_{W,1\text{-}6}|$ (note that the values of $D_{W,4}$ and $D_{W,6}$ were negative). The $E_\parallel$ and $E_{\parallel TD}$, and D_W are computed using the ($k_\parallel$, $k_\perp$) values corresponding to NRMSE$_{min}$ (red curves in Figures 4p–4q) during that interval, as well as the 10-s averages of the observed magnetic fields and plasma moments. The magnetic gradient scale $B_0/\nabla_\perp B$ estimated using the four MMS spacecraft with the linear gradient estimator technique (Chanteur, 1998; Chanteur & Harvey, 1998) is shown in Figure 6c. The values of $D_{W,1\text{-}6}$ summing up over k, the total D_W summing over $j = 1$–6, and $D_{W(LD+TD)}$ summing over $j = 1$, 3, and 5 are indicated on the right of Figure 6b. The largest effect was from the magnetic GD term ($D_{W,2}$) of $\sim 10^{11}$ m^2/s and the smallest effect was from the LD term ($D_{W,1}$) of $\sim 6 \times 10^8$ m^2/s. The total D_W for this interval was $\sim 10^{11}$ m^2/s, which is about an order of magnitude higher than $D_{W(LD+TD)}$ of $\sim 10^{10}$ m^2/s.

Figure 6d shows the temporal variation of the total D_W (red curve) and $D_{W(LD+TD)}$ (blue curve) across the separatrix using the ($k_\parallel$, $k_\perp$) values corresponding to NRMSE$_{min}$, as well as those with $<1.25 \times$ NRMSE$_{min}$ for uncertainty estimates. The importance of a diffusion process in the formation of a boundary layer has been evaluated by comparing it with the Bohm diffusion (Bohm, 1949; Treumann et al., 1995). The green curve in Figure 6d indicates the Bohm diffusion coefficient $D_{Bohm} = (1/16)k_B T_e/q_e B_0$, where k_B is Boltzmann's constant and q_e is the electron charge. The ion omnidirectional energy fluxes are plotted in Figure 6e for reference. Despite the diffusion rates being relatively lower without the effect of magnetic drift, both D_W and $D_{W(LD+TD)}$ became higher than D_{Bohm} after ∼04:24 UT, which approximately coincided with the start of two-component ions. The diffusion rates remained well above D_{Bohm} across the separatrix, thus indicating that cross-field diffusion can contribute to the observed mixing of cold low-latitude mantle ions and hot plasma sheet ions. Additionally, the density gradient in the Z direction, $\partial n/\partial z$, around the separatrix is estimated to be ~ 1–2×1 m^{-4} using the density differences between two MMS spacecraft that were separated mainly in the Z direction. Thus, the estimated particle flux across the separatrix due to diffusion, $D_W(\partial n/\partial z)$, is $\sim 10^{10}$–10^{11} m^{-2}s^{-1}.

4. MMS Event 2

We present in this section the summary results for event 2 on 19 August 2017. Figures 7a–7j give an overview of the event observed by MMS-3. During this event, as measured by ARTEMIS in the solar wind, IMF B_y remained positive at > 4 nT and IMF B_z was slightly positive (Figure 7a). MMS-3 was near the dusk flank at $X \sim -17$ R$_E$ and $Y \sim 16$ R$_E$ (see the locations at the bottom of Figure 7j). MMS was below the current sheet as indicated by the negative B_x in Figure 7b and crossed the separatrix at approximately 12:55–12:57 UT from the plasma sheet side to the lobe/mantle side (indicated on the top of Figure 7b). The same as event 1, the plasma sheet is defined by the appearance of isotropic electrons above 1 keV (Figure 7e). Strong fluctuations were seen in the electric field across the separatrix (Figure 7c). As seen in the ion omnidirectional energy spectrum shown in Figure 7d and the 1D distributions of omnidirectional ion energy fluxes and the 2D distributions of directional ion energy fluxes shown in Figures 7k–7n for three selected times (indicated by the vertical dotted lines in Figure 7d), MMS observed the two-component ions around the separatrix before ∼13:07 UT (see Figures 7k and 7m) and single-component cold low-latitude mantle ions afterward (see Figure 7n). The cool low-latitude mantle ion population had large N_i variations from ∼0.5 to up to 2 cm^{-3} (Figure 7f), $T_i \sim 0.1$ keV and $T_e \sim 0.02$ keV (Figure 7g),

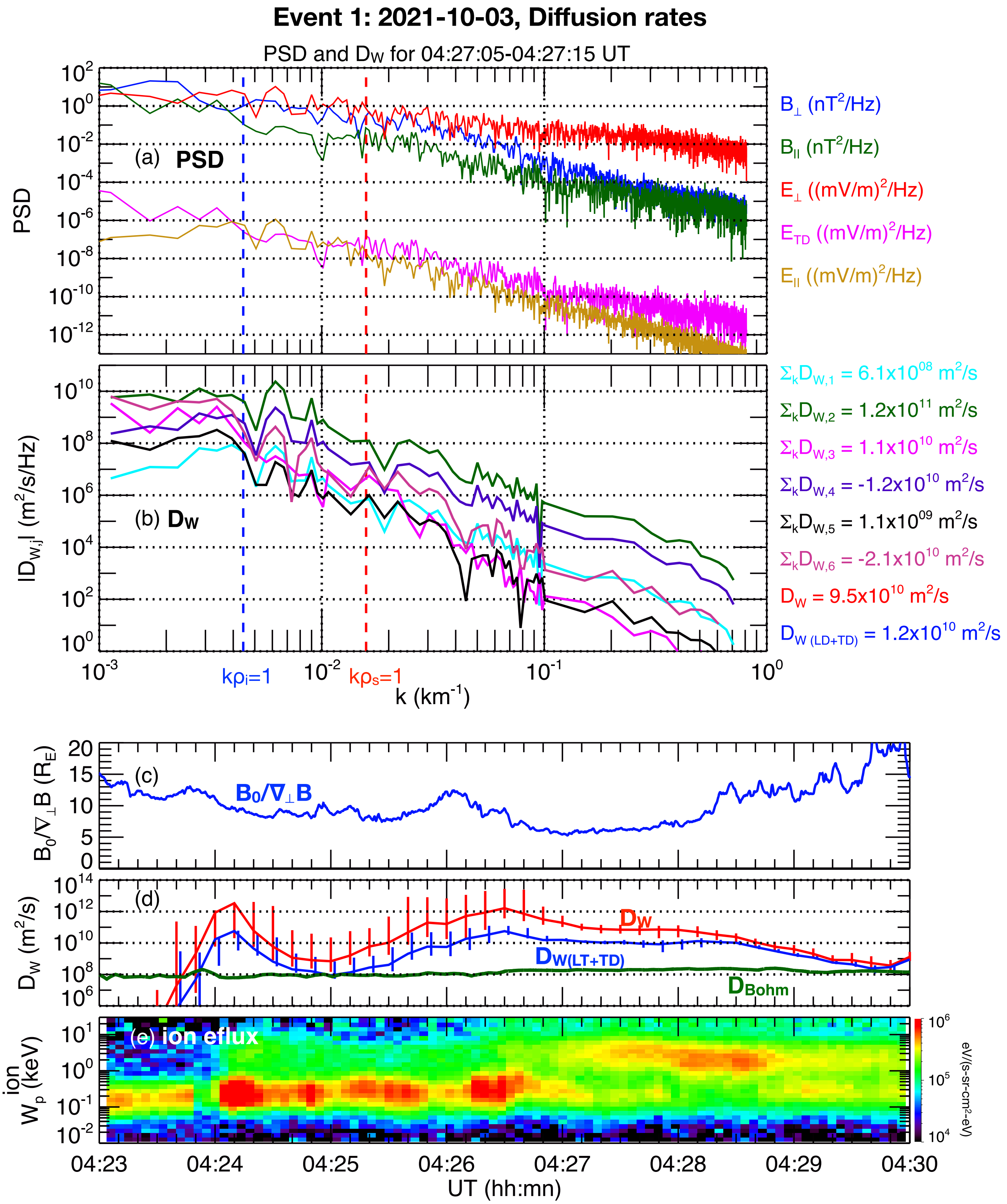

Figure 6. Diffusion rate estimation for Event 1 on 3 October 2021. (a) Power spectrum densitie of $B_\perp$, $B_\parallel$, $E_\perp$, $E_\parallel$ and $E_{\parallel TD}$, and (b) $|D_{w,1\text{-}6}|$ as a function of k for the 10-s interval of 04:27:05-04:27:15 UT. The blue and red vertical dashed lines indicate $k\rho_i = 1$ and $k\rho_s = 1$, respectively. Temporal variations from 04:23 to 04:30 UT for (c) $B_0/\nabla_\perp B$, (d) D_W (red), $D_{W(LD+TD)}$ (blue), and D_{Bohm} (green), and (e) energy spectrum of omnidirectional ion energy fluxes.

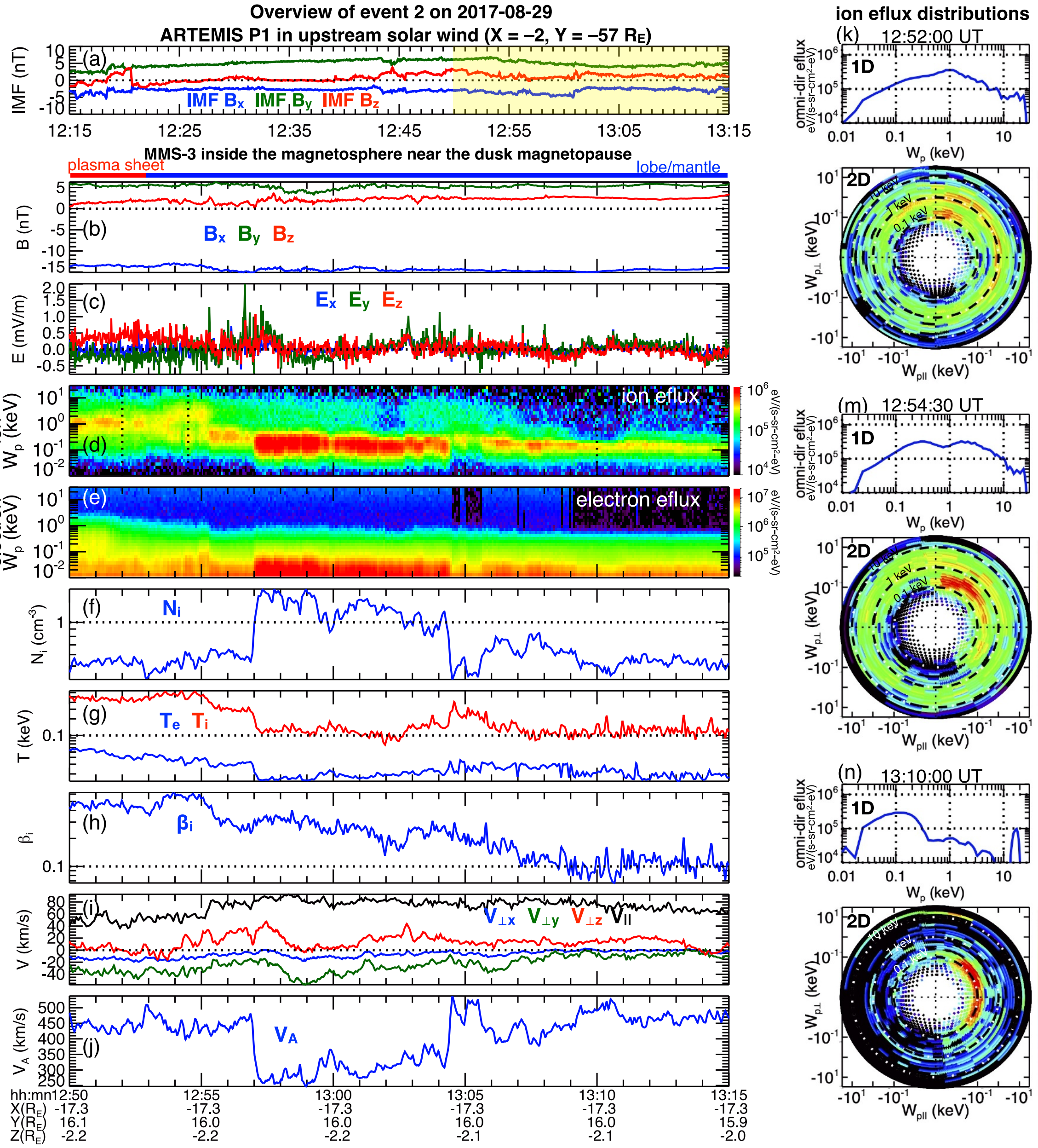

Figure 7. Overview of event 2 on 29 August 2017. (a) Interplanetary magnetic field observed by ARTEMIS P1. The yellow-shaded duration indicates the interval of event 2. (b–j) MMS-3 observations of panel (b) magnetic fields, (c) electric fields, energy spectrum of panel (d) ion and (e) electron omnidirectional energy fluxes, (f) ion density, (g) ion and electron temperatures, (h) ion plasma beta, (i) ion bulk perpendicular and parallel velocities, and (j) Alfvén speed. The regions encountered by MMS are indicated on the top by the blue (red) bars for lobe/mantle (plasma sheet). Ion energy flux distributions for three selected times (indicated by the three vertical dotted lines in panel (d)) at (k) 12:52:00, (m) 12:54:30, and (n) 13:10:00 UT shown as 1D distribution of omnidirectional energy fluxes (top) and 2D distribution of directional energy fluxes (bottom).

$\beta_i < \sim 0.3$ (Figure 7h), tailward field-aligned speed of >60 km/s (black line in Figure 7i), and large Alfvén speed varied from ~250 to 500 km/s (Figure 7j) corresponding to the density variations. In comparison, temperatures and β_i were relatively larger on the plasma sheet side due to the larger dominance of the hot-component population. Like event 1, the ions and electrons in the plasma sheet boundary during event 2 did not show the signatures indicating a magnetic field connection to a tail reconnection region.

Figure 8 summarizes the wave spectrum, estimated wave vectors, and diffusion rates for event 2 using the MMS-3 measurements. The temporal variations of the PSD of $B_\perp$, $E_\perp$, and $E_\perp/B_\perp/V_A$ ratio are shown in Figures 8a–8c,

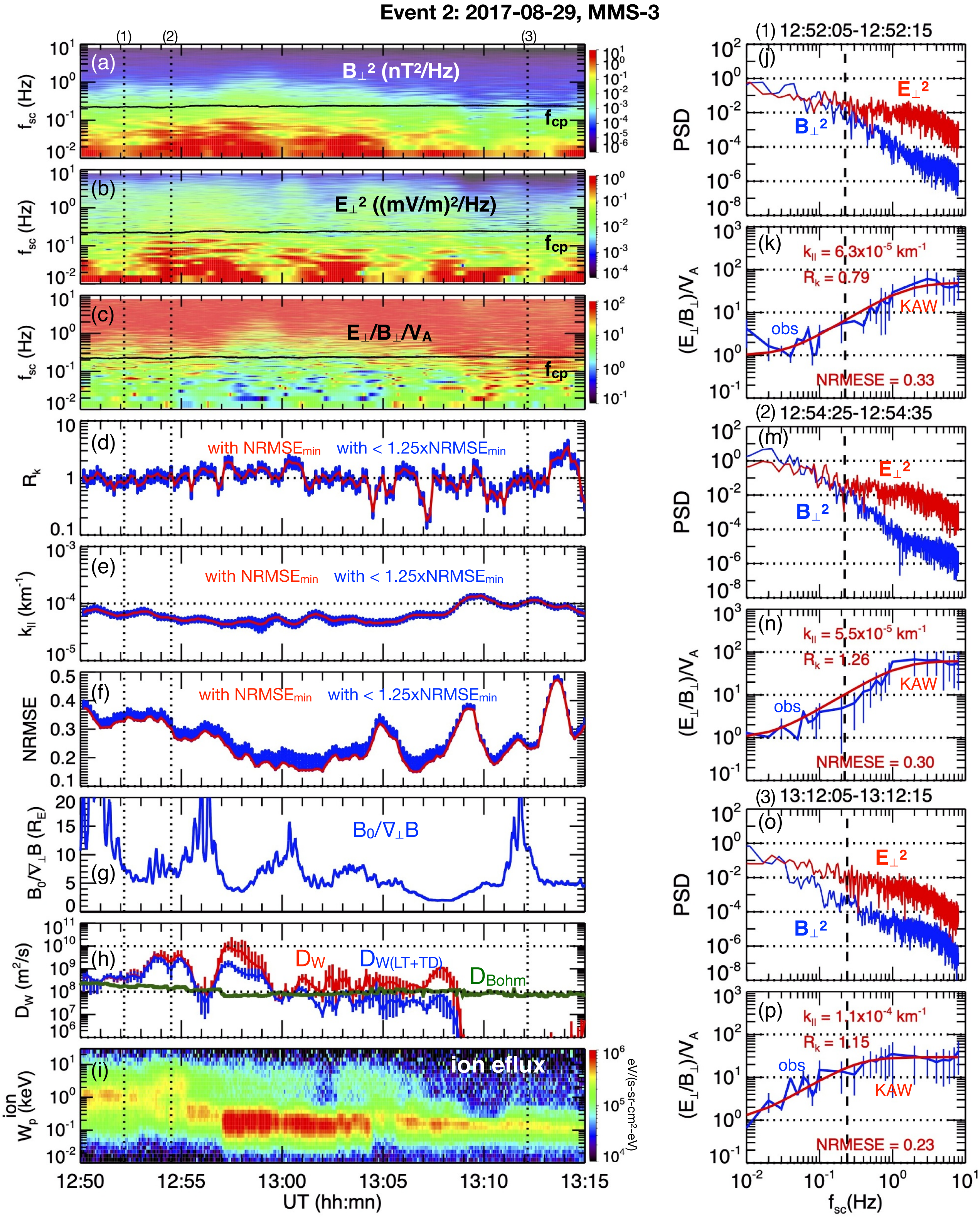
Event 2: 2017-08-29, MMS-3
(1) (2) (3)
(a) B⊥² (nT²/Hz)
(b) E⊥² ((mV/m)²/Hz)
(c) E⊥/B⊥/VA
fcp
fsc (Hz)
(d) Rk
(e) k|| (km⁻¹)
with NRMSEmin with < 1.25xNRMSEmin
(f) NRMSE
(g) B0/∇⊥B (RE)
(h) DW (m²/s)
DW DW(LT+TD) DBohm
(i) ion Wp (keV)
ion eflux
eV/(s-sr-cm²-eV)
12:50 12:55 13:00 13:05 13:10 13:15
UT (hh:mn)
(1) 12:52:05-12:52:15
(j) PSD E⊥² B⊥²
(k) k|| = 6.3x10⁻⁵ km⁻¹ Rk = 0.79 KAW obs NRMESE = 0.33
(E⊥/B⊥)/VA
(2) 12:54:25-12:54:35
(m) PSD E⊥² B⊥²
(n) k|| = 5.5x10⁻⁵ km⁻¹ Rk = 1.26 KAW obs NRMESE = 0.30
(3) 13:12:05-13:12:15
(o) PSD E⊥² B⊥²
(p) k|| = 1.1x10⁻⁴ km⁻¹ Rk = 1.15 KAW obs NRMESE = 0.23
fsc(Hz)

Figure 8.

respectively. The PSDs of $B_\perp$ and $E_\perp$ are compared in Figures 8j, 8m, and 8o for three selected 10-s intervals (1–3) (as indicated on the top of Figure 8a), respectively. Both the magnetic and electric field wave powers during intervals (1) and (2) on the plasma sheet side were relatively higher than those during interval (3) on the lobe/mantle side, but $E_\perp$ power remained higher than $B_\perp$ power at higher f_{sc} across the separatrix. The increasing $E_\perp/B_\perp/V_A$ ratio with increasing f_{sc} for the three intervals are shown in blue in Figures 8k, 8n, and 8p, respectively, which were close to the KAW dispersion shown in red with the estimated wave vectors and NRMSE values indicated (see Figure S2 in Supporting Information S1 for the comparison between R_{obs} and R_{KAW} for other intervals). The temporal variations of the estimated R_k, $k_\parallel$, and NRMSE values corresponding to NRMSE$_{min}$ (red) and their uncertainties (blue) are shown in Figures 8d–8f, respectively. Figure 8d shows that the Taylor hypothesis ($R_k \sim 1$) served as a good approximation for most of the time of this event. The magnetic gradient scale $B_0/\nabla_\perp B$ used in computing diffusion rates associated with GD is shown in Figure 8g. The temporal variations of the total D_W (red curve) and $D_{W(LD + TD)}$ (blue curve) across the separatrix using the ($k_\parallel$, $k_\perp$) values corresponding to NRMSE$_{min}$, as well as those with $<1.25 \times$ NRMSE$_{min}$ (uncertainty), are shown in Figure 8h, together with the D_{Bohm} variation (green). The magnitudes of $D_{W(LD + TD)}$ were smaller than those of D_W. Compared to the rates for event 1 shown in Figure 6, in event 2 the D_{Bohm} rates were similar but the magnitudes of D_W and $D_{W(LD + TD)}$ were smaller. Nevertheless, the D_W and $D_{W(LD + TD)}$ rates were still comparable to the D_{Bohm} rates across the separatrix until ∼13:09 UT, during which the mixing of the plasma sheet ions and the mantle ions was evident as shown in Figure 8i. Thus, the diffusion by KAWs plausibly played an important role in the cross-field transport.

5. Summary and Discussion

To understand the entry of the cool low-latitude mantle ions into the plasma sheet near the flanks under substantial IMF B_y, we investigated two MMS events around the separatrix (the interface between the plasma sheet and the lobe/mantle), to evaluate the role of the cross-field diffusive transport by KAWs. The key conclusions are the following.

1. Across the separatrix, the two-component mixing of hot plasma sheet ions with cool mantle ions was observed, indicating cross-field transport.
2. For the waves within $f_{sc} = 0.01$–10 Hz, the $E_\perp/B_\perp/V_A$ ratios were observed to increase with increasing f_{sc} and the ratios were quantitatively consistent with the KAW dispersion. This consistency allowed us to estimate wave vectors.
3. Our estimation of wave vectors, using either the fitting of the observed dispersion with KAWs or using the four-spacecraft timing method, shows that the Taylor hypothesis was a good approximation.
4. We estimate the cross-field diffusion rates for KAWs. The diffusion term due to magnetic field gradient drift was larger than others due to Landau damping associated with $E_\parallel$ and transient time damping associated with $B_\parallel$.
5. The estimated KAW diffusion rates were comparable to or higher than the Bohm diffusion rates during the intervals when the two-component mixing was observed, indicating plausibly that diffusive transport plays a role in the entry of low-latitude mantle ions into the plasma sheet.

In the evaluation of the KAW diffusion coefficients presented in this study, we only evaluate the effect of magnetic gradient drift since the theoretical predictions reported in previous studies did not include the curvature drift. For the two events presented here, around the tail separatrix the curvature scale was found to be comparable to the gradient scale and their directions were opposite to each other. Here we discuss qualitatively the likely contribution of the curvature drift. The curvature drift depends on the square of the parallel velocity, so the resonance condition no longer involves a simple Doppler shift of the magnetic drift of particles. When the curvature and gradient are in opposite directions, the resonant region of velocity space for the gradient and curvature drifts can be separated and distinct. It is expected that there will be two groups of resonant particles

Figure 8. Waves and diffusion rates based on MMS3 field fluctuations for event 2 on 29 August 2017. Power spectrum density (PSD) of panel (a) $B_\perp^2$, (b) $E_\perp^2$, and (c) the $E_\perp/B_\perp/V_A$ ratio as a function of f_{sc}. The black curves in (a–c) indicate the proton cyclotron frequency (f_{cp}). The three 10-s intervals (1)–(3) are indicated in the top of panel (a) and the wave spectrum are shown in panels (j–k) for interval (1), in panels (m–n) for interval (2), and in panels (o–p) for interval (3). (j, m, and o) The PSD of $B_\perp^2$ (blue) and $E_\perp^2$ (red). (k, n, and p) (k, n, and p) The $E_\perp/B_\perp/V_A$ ratio from observation (blue) and kinetic Alfvén wave (KAW) corresponding to NRMSE$_{min}$(red) with the $k_\parallel$, R_k, and NRMSE values indicated. Temporal variation of the estimated (d) R_K and (e) $k_\parallel$, and (f) their NRMSE for KAWs with NRMSE$_{min}$ (red) and $<1.25 \times$ NRMSE$_{min}$ (blue). Temporal variations of panel (g) $B_0/\nabla_\perp B$ and (h) D_W (red), $D_{W(LD + TD)}$ (blue), and D_{Bohm} (green). (i) Energy spectrum of ion omnidirectional energy fluxes.

corresponding to positive and negative wave numbers (e.g., the gradient drift corresponds to the positive mode while the curvature drift corresponds to the negative mode). While there may be some reduction in the diffusion coefficient of modes in a particular direction, the diffusion generally expands to include wave modes propagating in both directions, so again the overall contribution to diffusion is likely to remain similar. Still, it awaits the effect of the curvature drift to be theoretically predicted in the future so that it can be quantitatively evaluated with observations.

In this study, for the two-component ion mixing in the tail separatrix boundary we found that the Bohm diffusion rate was $\sim 10^8$ m^2/s while the observed KAWs can result in diffusion rates ranging from 10^8 to 10^{12} m^2/s. In comparison, for the two-component ion mixing in the low-latitude boundary layer along the flank magnetopause, the required diffusion rate is $\sim 10^9$ m^2/s (e.g., Sonnerup, 1980) and previous studies showed that the diffusion rates of $\sim 10^9$–10^{10}m^2/s can be generated by either KAWs (Chaston et al., 2008; Johnson & Cheng, 1997; Johnson & Wing, 2009) or the reconnection and diffusion associated with the Kevin-Helmholtz instability (Ma et al., 2017; Nykyri & Otto, 2001, 2004).

This study shows the effectiveness of diffusive transport primarily depends on the wave power of KAWs. The two events presented in this study only provide local observation, thus, we do not know whether the KAW diffusive transport was patchy or occurred across a large tail section. Even though we expect from the global simulation results (e.g., Wang et al., 2022) that the mantle plasma can be come into contact with the separatrix over a spatial scale of several R_E in the *Y* direction and even larger in the *X* direction, we need the spatial distributions of KAW power across the separatrix (cf. a similar study by Yao et al. (2011) at the magnetopause) in the future to evaluate the importance of KAW diffusion transport throughout the tail. Such spatial distributions will also help better understand the generation mechanisms and energy sources for KAWs around the separatrix. Other effects of KAWs, such as ion heating and resulting anisotropies (Johnson & Cheng, 2001) should also be considered in future studies.

In this study, the estimation of the diffusion rates relies on the wave vectors estimated by fitting KAW dispersion with the observed profiles. Despite that the MMS four-spacecraft configuration provides measurements that allow for direct estimation of wave vectors as a function of frequency, as has been conducted in several studies in the region of the magnetosheath with different multiple-spacecraft methods (e.g., Gershman et al., 2018; Hasegawa et al., 2020; Narita et al., 2016; Zhang et al., 2022), for our two events in the region of the magnetotail separatrix, we were only able to obtain such an estimation with good reliability within a limited frequency range for a few brief intervals with relatively larger field fluctuations. It is likely that the field fluctuations in the magnetosheath are stronger and more turbulent and broadband, thus more suitable for the application of these multiple-spacecraft methods. Nevertheless, in this study, we are still able to take advantage of it to conduct an independent evaluation of the Taylor hypothesis.

Data Availability Statement

The MMS data in CDF format for the four MMS spacecraft are available publicly online (https://lasp.colorado.edu/mms/sdc/public/data/). The ARTEMIS FGM data in CDF format for the two ARTEMIS spacecraft are available publicly online (http://themis.ssl.berkeley.edu/data/themis/thb/l2/fgm/ and https://themis.ssl.berkeley.edu/data/themis/thc/l2/fgm/).

Acknowledgments
C.-P. Wang is supported by NASA 80NSSC20K0714, 80NSSC22K1012, and NSF-GEM 2224108. J. Johnson is supported by NASA Grants 80NSSC22K0515, 80NNSC19J0843, and 80NSSC21K2009, and NSF AGS2131013. X. Xing is supported by NASA 80NSSC20K0714. L. Avanov is supported by NASA Magnetospheric Multiscale mission. H. Y. Wei is supported by UNH Subcontract #06-001. N. Ahmadi is supported by NASA Magnetospheric Multiscale mission. The authors acknowledge AS5-02099 for ARTEMIS and K. H. Glassmeier, U. Auster, and W. Baumjohann for the use of FGM data provided under DLR contract 50 OC 0302.

References

Angelopoulos, V. (2011). The ARTEMIS mission. *Space Science Reviews*, *165*(1–4), 3–25. https://doi.org/10.1007/s11214-010-9687-2
Ashour-Abdalla, M., Berchem, J. P., Büchner, J., & Zelenyi, L. M. (1993). Shaping of the magnetotail from the mantle: Global and local structuring. *Journal of Geophysical Research*, *98*(A4), 5651–5676. https://doi.org/10.1029/92JA01662
Auster, H. U., Glassmeier, K. H., Magnes, W., Aydogar, O., Baumjohann, W., Constantinescu, D., et al. (2008). The THEMIS fluxgate magnetometer. *Space Science Reviews*, *141*(1–4), 235–264. https://doi.org/10.1007/s11214-008-9365-9
Bohm, D. (1949). Quantitative description of the arc plasma in a magnetic field. In R. Walkerling (Ed.), *Characteristics of electrical discharges in magnetic fields A. Guthrie*, Chapter 3 (Vol. 1, p. 77). McGraw-Hil.
Chanteur, G. (1998). Spatial interpolation for four spacecraft: Theory. In G. Paschmann & P. W. Daly (Eds.), *Analysis methods for multi-spacecraft data* (pp. 349–370). ESA Publications Division.
Chanteur, G., & Harvey, C. C. (1998). Spatial Interpolation for four space-craft: Application to magnetic gradients. In G. Paschmann & P. W. Daly (Eds.), *Analysis methods for multi-spacecraft data* (pp. 371–394). SA Publications Division.
Chaston, C. C., Bonnell, J., McFadden, J. P., Carlson, C. W., Cully, C., Le Contel, O., et al. (2008). Turbulent heating and cross-field transport near the magnetopause from THEMIS. *Geophysical Research Letters*, *35*(17), L17S08. https://doi.org/10.1029/2008GL033601
Chaston, C. C., Bonnell, J. W., & Salem, C. (2014). Heating of the plasma sheet by broadband electromagnetic waves. *Geophysical Research Letters*, *41*(23), 8185–8192. https://doi.org/10.1002/2014GL062116

Chaston, C. C., Johnson, J. R., Wilber, M., Acuna, M., Goldstein, M. L., & Reme, H. (2009). Kinetic Alfvén wave turbulence and transport through a reconnection diffusion region. *Physical Review Letters*, *102*(1), 015001. https://doi.org/10.1103/PhysRevLett.102.015001
Chaston, C. C., Phan, T. D., Bonnell, J. W., Mozer, F. S., Acuna, M., Goldstein, M., et al. (2005). Drift-kinetic Alfvén waves observed near a reconnection X-line in the Earth's magnetopause. *Physical Review Letters*, *95*(6), 065002. https://doi.org/10.1103/physrevlett.95.065002
Crooker, N. U. (1992). Reverse convection. *Journal of Geophysical Research*, *97*(A12), 19363–19372. https://doi.org/10.1029/92JA01532
Fuselier, S. A., Lewis, W. S., Schiff, C., Ergun, R., Burch, J. L., Petrinec, S. M., & Trattner, K. J. (2016). Magnetospheric multiscale science mission profile and operations. *Space Science Reviews*, *199*(1–4), 77–103. https://doi.org/10.1007/s11214-014-0087-x
Gershman, D. J., F.-Viñas, A., Dorelli, J. C., Goldstein, M. L., Shuster, J., Avanov, L. A., et al. (2018). Energy partitioning constraints at kinetic scales in low- β turbulence. *Physics of Plasmas*, *25*(2), 022303. https://doi.org/10.1063/1.5009158
Gosling, J. T., Baker, D. N., Bame, S. J., Feldman, W. C., Zwickl, R. D., & Smith, E. J. (1985). North-South and dawn-dusk plasma asymmetries in the distant tail lobes: ISEE 3. *Journal of Geophysical Research*, *90*(A7), 6354–6360. https://doi.org/10.1029/JA090iA07p06354
Gosling, J. T., Baker, D. N., Bame, S. J., Hones, E. W., Jr., McComas, D. J., Zwickl, R. D., et al. (1984). Plasma entry into the distant tail lobes: ISEE-3. *Geophysical Research Letters*, *11*(10), 1078–1081. https://doi.org/10.1029/GL011i010p01078
Grzedzielski, S., & Macek, W. (1988). An open magnetopause model of the Earth's distant tail based on ISEE 3 evidence. *Journal of Geophysical Research*, *93*(A3), 1795–1808. https://doi.org/10.1029/JA093iA03p01795
Haerendel, G., & Paschmann, G. (1975). Entry of solar wind plasma into the magnetosphere. In B. Hultqvist & L. Stenflo (Eds.), *Physics of the hot plasma in the magnetosphere* (pp. 23–43). Plenum.
Hardy, D. A., Freeman, J. W., & Hills, H. K. (1976). Plasma observations in the magnetotail. In B. M. McCormac (Ed.), *Magnetospheric particles and fields* (Vol. 89, pp. 89–98). D. Reidel. https://doi.org/10.1007/978-94-010-1503-5_9
Hardy, D. A., Hills, H. K., & Freeman, J. W. (1975). A new plasma regime in the distant geomagnetic tail. *Geophysical Research Letters*, *2*(5), 169–172. https://doi.org/10.1029/GL002i005p00169
Hardy, D. A., Hills, H. K., & Freeman, J. W. (1979). Occurrence of the lobe plasma at lunar distance. *Journal of Geophysical Research*, *84*(A1), 72–78. https://doi.org/10.1029/JA084iA01p00072
Hasegawa, A., & Mima, K. (1978). Anomalous transport produced by kinetic Alfvén wave turbulence. *Journal of Geophysical Research*, *83*(A3), 1117–1123. https://doi.org/10.1029/JA083iA03p01117
Hasegawa, H., Nakamura, T. K. M., Gershman, D. J., Nariyuki, Y., Viñas, A. F., Giles, B. L., et al. (2020). Generation of turbulence in Kelvin-Helmholtz vortices at the Earth's magnetopause: Magnetospheric multiscale observations. *Journal of Geophysical Research: Space Physics*, *125*(3), e2019JA027595. https://doi.org/10.1029/2019JA027595
Johnson, J. R., & Cheng, C. Z. (1997). Kinetic Alfvén waves and plasma transport at the magnetopause. *Geophysical Research Letters*, *24*(11), 1423–1426. https://doi.org/10.1029/97GL01333
Johnson, J. R., & Cheng, C. Z. (2001). Stochastic ion heating at the magnetopause due to kinetic Alfvén waves. *Geophysical Research Letters*, *28*(23), 4421–4424. https://doi.org/10.1029/2001gl013509
Johnson, J. R., & Wing, S. (2009). Northward interplanetary magnetic field plasma sheet entropies. *Journal of Geophysical Research*, *114*(A9), A00D08. https://doi.org/10.1029/2008JA014017
Li, W., Raeder, J., Dorelli, J., Øieroset, M., & Phan, T. D. (2005). Plasma sheet formation during long period of northward IMF. *Geophysical Research Letters*, *32*(12), L12S08. https://doi.org/10.1029/2004GL021524
Li, W., Raeder, J., Øieroset, M., & Phan, T. D. (2009). Cold dense magnetopause boundary layer under northward IMF: Results from THEMIS and MHD simulations. *Journal of Geophysical Research*, *114*(A1), A00C15. https://doi.org/10.1029/2008JA013497
Ma, X., Delamere, P., Otto, A., & Burkholder, B. (2017). Plasma transport driven by the three-dimensional Kelvin-Helmholtz instability. *Journal of Geophysical Research: Atmospheres*, *122*(10), 10382–10395. https://doi.org/10.1002/2017JA024394
Maezawa, K., & Hori, T. (1998). The distant magnetotail: Its structure, IMF dependence, and thermal properties. In A. Nishida, D. N. Baker, & S. W. H. Cowley (Eds.), *New perspectives on the Earth's magnetotail*, *Geophysical Monograph Series* (Vol. 105, pp. 1–20). American Geophys. Union.
Narita, Y., Plaschke, F., Nakamura, R., Baumjohann, W., Magnes, W., Fischer, D., et al. (2016). Wave telescope technique for MMS magnetometer. *Geophysical Research Letters*, *43*(10), 4774–4780. https://doi.org/10.1002/2016GL069035
Nykyri, K., & Otto, A. (2001). Plasma transport at the magnetospheric boundary due to reconnection in Kelvin-Helmholtz vortices. *Geophysical Research Letters*, *28*(18), 3565–3568. https://doi.org/10.1029/2001GL013239
Nykyri, K., & Otto, A. (2004). Influence of the Hall term on KH instability and reconnection inside KH vortices. *Annales de Geophysique*, *22*(3), 935–949. https://doi.org/10.5194/angeo-22-935-2004
Otto, A., & Fairfield, D. H. (2000). Kelvin-Helmholtz instability at the magnetotail boundary: MHD simulation and comparison with Geotail observations. *Journal of Geophysical Research*, *105*(A9), 21175–21190. https://doi.org/10.1029/1999JA000312
Pilipp, W. G., & Morfill, G. (1978). The formation of the plasma sheet resulting from plasma mantle dynamics. *Journal of Geophysical Research*, *83*(A12), 5670–5678. https://doi.org/10.1029/JA083iA12p05670
Pollock, C., Moore, T., Jacques, A., Burch, J., Gliese, U., Saito, Y., et al. (2016). Fast plasma investigation for magnetospheric multiscale. *Space Science Reviews*, *199*(1–4), 331–406. https://doi.org/10.1007/s11214-016-0245-4
Raeder, J., Walker, R. J., & Ashour-Abdalla, M. (1995). The structure of the distant geomagnetic tail during long periods of northward IMF. *Geophysical Research Letters*, *22*(4), 349–352. https://doi.org/10.1029/94gl03380
Russell, C. T., Mellott, M. M., Smith, E. J., & King, J. H. (1983). Multiple spacecraft observations of interplanetary shocks: Four spacecraft determination of shock normals. *Journal of Geophysical Research*, *88*(A6), 4739–4748. https://doi.org/10.1029/JA088iA06p04739
Schwartz, S. J. (1998). Shock and discontinuity normals, Mach numbers, and related parameters. *ISSI Scientific Reports Series*, *1*, 249–270.
Sergeev, V. A., Apatenkov, S. V., Nakamura, R., Plaschke, F., Baumjohann, W., Panov, E. V., et al. (2021). MMS observations of reconnection separatrix region in the magnetotail at different distances from the active neutral X-line. *Journal of Geophysical Research: Space Physics*, *126*(2), e2020JA028694. https://doi.org/10.1029/2020JA028694
Sibeck, D. G., Angelopoulos, V., Brain, D. A., Delory, G. T., Eastwood, J. P., Farrell, W. M., et al. (2011). ARTEMIS science objectives. *Space Science Reviews*, *165*(1–4), 59–91. https://doi.org/10.1007/s11214-011-9777-9
Sibeck, D. G., & Lin, R.-Q. (2014). Size and shape of the distant magnetotail. *Journal of Geophysical Research: Space Physics*, *119*(2), 1028–1043. https://doi.org/10.1002/2013JA019471
Siscoe, G. L., Frank, L. A., Ackerson, K. L., & Paterson, W. R. (1994). Properties of mantle-like magnetotail boundary layer: Geotail data compared with a mantle model. *Geophysical Research Letters*, *21*(25), 2975–2978. https://doi.org/10.1029/94gl01601
Siscoe, G. L., & Sanchez, E. (1987). An MHD model for the complete open magnetotail boundary. *Journal of Geophysical Research*, *92*(A7), 7405–7412. https://doi.org/10.1029/JA092iA07p07405

Sonnerup, B. (1980). Theory of the low-latitude boundary layer. *Journal of Geophysical Research*, *85*(A5), 2017–2026. https://doi.org/10.1029/ja085ia05p02017

Taguchi, S., Kishida, H., Mukai, T., & Saito, Y. (2001). Low-latitude plasma mantle in the near-Earth magnetosphere: Geotail observations. *Journal of Geophysical Research*, *106*(A2), 1978–2012. https://doi.org/10.1029/2000ja900100

Tooley, C. R., Black, R. K., Robertson, B. P., Stone, J. M., Pope, S. E., & Davis, G. T. (2016). The magnetospheric multiscale constellation. *Space Science Reviews*, *199*(1–4), 23–76. https://doi.org/10.1007/s11214-015-0220-5

Torbert, R. B., Russell, C. T., Magnes, W., Ergun, R. E., Lindqvist, P.-A., LeContel, O., et al. (2016). The FIELDS instrument suite on MMS: Scientific objectives, measurements, and data products. *Space Science Reviews*, *199*(1-4), 105–135. https://doi.org/10.1007/s11214-014-0109-8

Trainer, K. J., Petrinec, S. M., & Fuselier, S. (2021). The location of magnetic reconnection at Earth's Magnetopause. *Space Science Reviews*, *217*(3), 41. https://doi.org/10.1007/s11214-021-00817-8

Treumann, R. A., Labelle, J., & Bauer, T. M. (1995). Diffusion processes: An observational perspective. In *Geophysical Monograph series* (Vol. 90, pp. 331–341). American Geophysical Union. https://doi.org/10.1029/gm090p0331

Wang, C.-P., Lyons, L. R., & Angelopoulos, V. (2014). Properties of low-latitude mantle plasma in the Earth's magnetotail: ARTEMIS observations and global MHD predictions. *Journal of Geophysical Research: Space Physics*, *119*(9), 7264–7280. https://doi.org/10.1002/2014JA020060

Wang, C.-P., & Xing, X. (2021). Solar wind entry into midtail current sheet via low-latitude mantle under dominant IMF b_y: ARTEMIS observation. *Journal of Geophysical Research: Space Physics*, *126*(9), e2021JA029402. https://doi.org/10.1029/2021JA0294

Wang, C.-P., Xing, X., Wang, X., Avanov, L. A., Lin, Y., Strangeway, R. J., & Wei, H. Y. (2022). Effect of IMF b_y on the entry of solar wind ions into the near-Earth tail lobe: Global hybrid simulation and MMS observation. *Journal of Geophysical Research: Space Physics*, *127*(9), e2022JA030800. https://doi.org/10.1029/2022JA030800

Wellenzohn, S., Nakamura, R., Nakamura, T. K. M., Varsani, A., Sergeev, V. A., Apatenkov, S. V., et al. (2021). Remote sensing of magnetic reconnection in the magnetotail using in situ multipoint observations at the plasma sheet boundary layer. *Journal of Geophysical Research: Space Physics*, *126*(1), e2020JA028917. https://doi.org/10.1029/2020JA028917

Wing, S., Johnson, J. R., Chaston, C. C., Echim, M., Escoubet, C. P., Lavraud, B., et al. (2014). Review of solar wind entry into and transport within the plasma sheet. *Space Science Reviews*, *184*(1–4), 33–86. https://doi.org/10.1007/s11214-014-0108-9

Yao, Y., Chaston, C. C., Glassmeier, K.-H., & Angelopoulos, V. (2011). Electromagnetic waves on ion gyro-radii scales across the magnetopause. *Geophysical Research Letters*, *38*(9), L09102. https://doi.org/10.1029/2011GL047328

Zhang, W. Z., Fu, H. S., Cao, J. B., Liu, Y. Y., Zhao, J. S., Guo, Z. Z., et al. (2022). Draft: A method for wave analyses in space plasmas. *The Astrophysical Journal*, *936*(2), 176. https://doi.org/10.3847/1538-4357/ac8872